

Kenneth L. Pryor
Center for Satellite Applications and Research (NOAA/NESDIS)
College Park, MD

1. INTRODUCTION

The launch of Geostationary Operational Environmental Satellite (GOES)-16 in November 2016 and subsequent activation of the Advanced Baseline Imager (ABI) in January 2017 has resulted in the increased accessibility to high spatial and temporal satellite image datasets for convective storm monitoring and nowcasting. The existing suite of GOES downburst prediction algorithms employs the GOES imager and sounder to calculate potential of occurrence based on conceptual models of favorable environmental thermodynamic profiles for downburst generation. Traditional meteorological satellite techniques for deep convective storm monitoring, including the water vapor – longwave infrared (WV – IR) brightness temperature difference (BTD), have recently been extended by multichannel techniques for diagnosing attributes of a favorable downburst environment. The WV-IR BTD has demonstrated the ability to infer convective storm structure signatures that signify the occurrence of hazardous conditions that entail large hail and severe and potentially damaging straight-line winds resulting from downbursts, and, with 2-km resolution GOES-16 ABI data, the BTD product is able to detect fine detail signatures more effectively when compared to 4-km resolution GOES-13-15 imagery. Accordingly, a three-channel BTD algorithm incorporating split window IR channels (11 μ m, 12 μ m) and a WV channel (6.7 μ m) produces an output BTD that is proportional to downburst potential and supplements the sounder-derived Microburst Windspeed Potential Index (MWPI)(Pryor 2014, Pryor 2015) that is designed to diagnose attributes of a favorable downburst environment:

1) the presence of convective available potential energy (CAPE), and 2) the presence of a deep surface-based or elevated mixed layer with a large temperature lapse rate.

The three-channel GOES imager product (Pryor 2009) has been developed and experimentally implemented to assess downburst potential over the western United States with improved temporal and spatial resolution. The availability of the split-window channel in the GOES-16 imager allows for the inference of boundary layer moisture content. Wakimoto (1985), based on his study of microbursts that occurred during the Joint Airport Weather Studies (JAWS) project, noted favorable environmental conditions over the western United States: (1) intense solar heating of the surface and a resulting superadiabatic surface layer; (2) a deep, dry-adiabatic convective boundary layer (Sorbjan 1989) that extends upward to near the 500mb level; (3) a well-mixed moisture profile with a large relative humidity gradient between the mid-troposphere and the surface. The GOES-16 ABI microburst algorithm employs brightness temperature differences (BTD) between band 10 (lower-middle level water vapor, 7.3 μ m), band 14 (longwave infrared window, 11 μ m), and split window band 15 (12 μ m). Band 10 is intended to indicate lower to middle tropospheric moisture content and advection while band 15 indicates surface layer moisture content. Soden and Bretherton (1996) (SB96), in their study of the relationship of water vapor radiance and layer-average relative humidity, found a strong negative correlation between 7.3 μ m brightness temperature (T_b) and layer-averaged relative humidity (RH) between the 300 and 700-mb levels. Thus, in the middle troposphere, decreases in T_b are associated with increases in RH as illustrated in Figure 4 of SB96. It follows that large BTD between bands 10 and 15 imply a large relative humidity gradient between the mid-troposphere and the surface, a condition favorable for strong convective downdraft generation due to evaporational cooling in the sub-cloud layer. In contrast, a positive BTD between bands 14 and 15 indicates a relatively moist surface layer. Thus, the GOES imager microburst risk (MBR) product is based on the following algorithm in which the output brightness temperature difference (BTD) is proportional to microburst potential:

*Corresponding author address: Kenneth L. Pryor, NOAA/NESDIS/STAR, 5830 University Research Ct., College Park, MD 20740; e-mail: Ken.Pryor@noaa.gov.

$$\text{MBR (BTD)} = \{T_{15} - T_{10}\} + \{T_{14} - T_{15}\} \quad (1)$$

Where the parameter T_n represents the brightness temperature observed in a particular imager band. The relationship between BTD and microburst risk in the product image is based on the following assumptions: (1) A deep, well-mixed convective boundary layer exists in the region of interest; (2) moisture for convective storm development is based in the mid-troposphere and is advected over the region of interest; and (3) the mid- to upper- tropospheric layer of moisture is vertically extensive and would yield precipitation if provided a sufficient forcing mechanism. The importance of the $\{T_{14} - T_{15}\}$ term derives from the contribution of a surface-based moist layer in the enhancement of downdraft acceleration. Srivastava (1985) noted that lower environmental relative humidity in the boundary layer, a condition typically associated with an inverted-V thermodynamic profile, has a detrimental effect on downdraft intensity because of the lowering of virtual temperature and the resultant decrease in the virtual temperature deficit between the evaporatively cooled downdraft and the surrounding environment. Assuming that evaporation continues to sustain the downdraft with approach to the surface, increased water vapor content in the surface layer will increase the environmental virtual temperature and the resultant deficit, and thereby reinforce negative buoyancy and downdraft acceleration.

This product provides a higher spatial (2 km) and temporal (5 minutes) resolution than is currently offered by the GOES sounder microburst products (10 km, 60 minutes) and thus, provides useful information to supplement the sounder products in the convective storm nowcasting process. In addition, this imager product provides microburst risk guidance in high latitude regions, especially north of latitude 50°N, where existing sounder coverage is not available. Both the GOES sounder MWPI and imager microburst risk products were developed as predictive linear models developed in the manner exemplified in Caracena and Flueck (1988). Each microburst product consists of a set of predictor variables that generates output of expected microburst risk.

The traditional usage of the brightness temperature difference (BTD) between GOES infrared channel 3 (WV, 6.5 μm) and channel 4 (IR, 11 μm) is the monitoring of convective storm intensity by detection of overshooting thunderstorm tops. Rabin et.al. (2017) noted

observations that have shown positive BTD ($> 0^\circ\text{K}$) can occur when water vapor exists above cloud tops in a stably stratified lower stratosphere due forced ascent from overshooting tops. Thus, a BTD greater than zero (0°K) has been used a measure for intensity of overshooting convection. In addition, Schmetz et al. (1997) associated a positive BTD with a deep convective storm cloud top that has reached the height of the tropopause and lower stratosphere. A threshold BTD of $> -10^\circ\text{C}$ indicates the presence of mature convective clouds, with tops approaching the upper troposphere that will soon likely generate precipitation (Mecikalski and Bedka 2006). An alternative application of the WV-IR BTD technique was proposed by Pryor (2014) based on a conceptual model of a dry-air “notch” that was formulated to represent unsaturated air that intrudes into a convective storm and interacts with convective and stratiform precipitation regions, subsequently providing the energy for intense downdrafts and resulting outflow winds. Figure 1 graphically describes the physical process of downburst generation within a local storm. The presence of a dry-air “notch” on the periphery of a convective storm suggests, on the local storm scale, direct interaction of unsaturated air with the precipitation core that results from wake entrainment as described by Knupp (1989). Through numerical simulations, the author confirmed that entrainment of dry mid-level air into the downshear flank of a convective storm fostered strong downdraft generation.

This paper presents an updated assessment of the imager and sounder-derived algorithms applied to GOES-16 ABI data featuring case studies that demonstrate the effective use of cloud and moisture imagery with 13-km Rapid Refresh (RAP) model data to simulate advanced sounder-derived products. In addition, the sounder and imager microburst products will be compared and contrasted, and this paper will outline the advantages of each product in the nowcasting process.

2. METHODOLOGY

The objective of this validation effort was to qualitatively and quantitatively assess the performance of the GOES MWPI product and imager-derived microburst products by employing classical statistical analysis of real-time data. Accordingly, this effort entailed a study of downburst events over the Eastern Snake River Plain (ESRP) of southeastern Idaho during the 2017 convective season that was executed in

a manner that emulates historic field projects such as the 1982 Joint Airport Weather Studies (JAWS) (Wakimoto 1985). GOES-16 ABI Cloud and Moisture Imagery product (CMIP) datasets was collected for pre-convective and convective environments associated with a severe downburst event that occurred within the Idaho National Laboratory (INL) mesonet domain on 4 June 2017. Clawson et al. (2007) provides a detailed climatology and physiographic description of the INL as well as a description of the associated mesonet network. Wakimoto (1985) discussed the effectiveness of using mesonet surface observations and radar reflectivity data in the verification of the occurrence of downbursts. Well-defined peaks in wind speed (Wakimoto 1985) were effective indicators of downburst occurrence.

As shown in Figure 2, GOES-16 product images were generated by Python programs where GOES imager ABI brightness temperature data was read and processed, and output BT values were mapped using the Python 2D plotting library (Matplotlib, <https://matplotlib.org/>). The image data consisted of derived brightness temperatures from ABI infrared bands 10, 14, and 15, obtained from the NESDIS/STAR Central Data Repository (SCDR). The RAOB thermodynamic profile shown in Figure 3 was generated by the Sounding/Hodograph Analysis and Research Program in Python (SHARPPy, <https://github.com/sharppy/SHARPPy>). SHARPPy is a collection of open source sounding and hodograph analysis routines.

Downburst wind gusts, as recorded by National Oceanic and Atmospheric Administration (NOAA) mesonet observation stations, were measured at a height of 15 meters (50 feet) above ground level. Archived NOAA mesonet observations are available via the NOAA INL Weather Center website (<http://niwc.noaa.inel.gov>). In order to assess the predictive value of the GOES-derived microburst products, the images used in validation were obtained for valid times one to three hours prior to the observed surface wind gusts. Derived images generated from the infrared dataset consisted of (1) band 14-15 difference image; (2) three-channel BT (microburst risk) image and (3) WV-IR BT image. In addition, based on the statistical relationship derived between output BT and observed downburst wind gust speed, a color-enhanced risk image was generated that indicates increasing microburst potential as a progression from yellow to red shading. Example transmittance weighting functions for bands 10,

14, and 15 that specify the relative contribution from each atmospheric layer to emitted radiation were obtained for southeastern Idaho in the vicinity of INL from a Cooperative Institute for Meteorological Satellite Studies (CIMSS) website (<http://cimss.ssec.wisc.edu/goes/wf/index.php>).

The weighting functions were compared to temperature and moisture profiles in the 0000 UTC Salt Lake City, Utah RAOB and product imagery for selected microburst events that occurred during the late afternoon hours (between 2200 and 0000 UTC 5 June 2017). Thus, the group of spectral bands selected to detect radiation emitted from layers of interest in the atmosphere could be determined to be most effective for temperature and moisture profiling for the purpose of inferring the presence of a favorable environment for microbursts.

For each microburst event, product images were compared to radar reflectivity imagery and surface observations of convective wind gusts as provided by INL mesonet stations. Next Generation Radar (NEXRAD) base reflectivity imagery (levels II and III) from National Centers for Environmental Information (NCEI) and University Corporation for Atmospheric Research (UCAR) THREDDS server was utilized to verify that observed wind gusts were associated with downbursts and not associated with other types of convective wind phenomena (i.e. gust fronts). Another application of the NEXRAD imagery was to infer microscale physical properties of downburst-producing convective storms. Particular radar reflectivity signatures, such as the rear-inflow notch (RIN) (Przybylinski 1995) and the spearhead echo (Fujita and Byers 1977), were effective indicators of the occurrence of downbursts. In addition, radar temperature profiles over the INL, generated at Grid3 mesonet station, were archived as a means to validate quantitative information as portrayed in the derived product images.

Covariance between the variables of interest, MWPI and the three-channel BT, and surface downburst wind gust speed, was analyzed to assess the performance of the downburst prediction algorithms. An effective means to quantify the functional relationship between microburst index algorithm output and downburst wind gust strength at the surface was to apply and compare linear and non-linear regression techniques, and compute root mean square error (RMSE) and correlation between these variables.

3. CASE STUDY: IDAHO DOWNBURSTS

During the afternoon of 4 June 2017, strong thunderstorms developed along a cold front over the northwestern United States and produced severe winds over southern Idaho and in the Salt Lake City, Utah area. Ahead of the cold front, a deep convective mixed layer was established, as apparent by the presence of a classic “inverted-V” thermodynamic profile in the 0000 UTC 5 June RAOB over Salt Lake City, Utah shown in Figure 3. The large temperature lapse rate in the deep subcloud layer below the 500 mb level fostered strong downdraft instability, which is echoed in Figure 4 by the large 500 – 700 mb lapse rates ($> 9 \text{ }^\circ\text{C/km}$) over southeastern Idaho and Utah calculated from RAP model data three hours prior at 2100 UTC. The thermodynamic profile also effectively displayed a surface-based moist layer that was co-located with the storm effective inflow layer, suggesting that a marginal amount of moist air was available for the development of deep precipitating convection. Comparison of the SLC RAOB to a co-located GOES-15 sounder-derived vertical profile shown in Figure 3 revealed that the GOES sounding closely echoed the inverted-V pattern displayed in the RAOB.

Pooling of low level moisture along the cold front, as evidenced by elevated dew point values (not shown) along a zone extending from Idaho Falls to Pocatello and Twin Falls, resulted in elevated CAPE values immediately east of the INL. This condition established a large MWPI gradient (4 – 5) within the storm inflow region and wind gust potential of 50 to 55 knots. Downburst-related wind gusts of 52 to 54 knots were recorded by NOAA Air Resources Laboratory (ARL) wind sensors at the Idaho National Laboratory (INL) between 2255 and 2325 UTC. Figures 5 and 7 display GOES-16 imagery, generated by Python software, for the 4 June severe weather outbreak, and show a high level of detail in storm structure and environment as compared to GOES-15 imagery shown in Figure 6. The GOES-16 three-channel brightness temperature difference (BTD) product demonstrated the ability to indicate severe wind gust potential (>50) immediately downstream of the evolving multicell thunderstorm as it tracked over the INL. Also interesting was the effectiveness of the corresponding water vapor (WV) – infrared (IR) channel BTD imagery in Figure 7 to show favorable storm structure signatures associated with downburst producing thunderstorms (i.e. cold storm cloud tops (red-

white shading) and dry-air notches) at least ten minutes prior to the appearance of a bow echo in NEXRAD imagery in Figure 8. Inspection of Figures 7 and 8 revealed a combination of cold storm cloud tops ($> -10^\circ\text{C}$) and moderate radar reflectivity factor ($Z \sim 35 \text{ dBZ}$) that suggested the favorability for strong storm updrafts occurring in an environment with modest lower tropospheric moisture that could result in a precipitation core dominated by a higher concentration of smaller ice particles (i.e. graupel, aggregates). Srivastava (1987) found that a high concentration of smaller particles, both ice and liquid, further enhances downdraft intensity and noted that in the case of two storms with similar precipitation content, the storm with a higher concentration of smaller particles produces a stronger downdraft. INL surface wind observations plotted in Figure 9 confirm downburst occurrence as a divergent wind pattern superimposed on the southerly environmental wind flow.

4. STATISTICAL ANALYSIS AND DISCUSSION

Analysis of covariance between the variables of interest (MWPI and three-channel BTD) and surface downburst wind gust speed, provided favorable results as shown in Figure 10. As illustrated in the scatterplot diagrams, microburst risk values do not represent absolute wind gust speeds, but rather indicate relative convective wind gust potential that can be statistically related by the process of regression to surface wind gust speed. Similar to the imager microburst product, the MWPI product was originally developed as a linear predictive model. However, nonlinear regression has more recently demonstrated that quadratic equations more effectively represent wind gust potential derived from the BTD and MWPI products, as evidenced by generally lower RMSE values. The regression approach allows the user to tune the relationship between risk values and downburst wind gust speeds according to local climatology. One important goal of this validation effort was to derive a relationship between MWPI and BTD values, and categories of microburst wind gust potential (i.e. <35 knots, 35-49 knots, 50-64 knots, etc.) employing both linear and non-linear regression.

Documentation of microbursts in the INL mesonet domain revealed that microburst activity occurred primarily during the afternoon. This preference for afternoon microburst activity underscores the importance of solar heating of

the boundary layer in the process of convective downdraft generation over southeastern Idaho, especially in the presence of a mesoscale forcing mechanism such as a cold front. The well-mixed moisture profile and relative humidity gradient that results from diurnal heating fostered a favorable environment for microbursts that would occur due to the evaporation of precipitation in the dry sub-cloud layer. Water vapor satellite imagery, RAOBs and GOES sounding profiles provided evidence that significant mid-level moisture promoted precipitation loading as an initiating mechanism for downbursts over the INL domain. The combination of precipitation loading and the presence of a relatively deep and dry convective boundary layer favored a microburst environment that was effectively captured by the GOES imager-derived microburst product. Thus, derivation of an algorithm that incorporates the previous GOES-11 bands 3, 4, and 5 and applies to GOES-16 ABI water vapor and split-window longwave infrared channels appears to be effective in indicating a favorable thermodynamic environment for microbursts over southeastern Idaho as well as other regions in the intermountain western U.S.

5. SUMMARY AND CONCLUSIONS

As documented in this paper, and proven by statistical analysis, the GOES sounder MWPI and the multispectral GOES imager products have demonstrated the ability to assess downburst potential over the western United States. Case studies and statistical analysis for downburst events that occurred over southeastern Idaho during the 2007 and 2008 convective seasons and over the U.S. Great Basin region between 2013 and 2015 demonstrated the effectiveness of the imager product with a significant correlation between risk values and microburst wind gust magnitude. The GOES-11 imager microburst product was previously found to be effective in indicating the potential for dry microbursts. Applied to GOES-16 ABI data for the 4 June 2017 northwestern U.S. downburst event, the WV – IR and three-channel BTD products provide a higher level of detail in thermodynamic and storm structure. Caracena and Flueck (1988) found that the majority of microburst days during JAWS were characterized by environments intermediate between the dry and wet extremes (i.e. hybrid). Accordingly, as noted in Pryor (2014, 2015) and in this paper, the MWPI and three-channel BTD products are especially useful in the inference of the presence

of intermediate or “hybrid” microburst environments, especially over the Great Plains and Great Basin regions.

6. REFERENCES

- Caracena, F., and J.A. Flueck, 1988: Classifying and forecasting microburst activity in the Denver area. *J. Aircraft*, **25**, 525-530.
- Clawson, K.L., N.R. Ricks, and G.E. Start, 2007: Climatology of the Idaho National Engineering Laboratory. Department of Energy, 169 pp.
- Fujita, T.T., 1971: Proposed characterization of tornadoes and hurricanes by area and intensity. SMRP Research Paper 91, University of Chicago, 42 pp.
- Fujita, T.T., and H.R. Byers, 1977: Spearhead echo and downburst in the crash of an airliner. *Mon. Wea. Rev.*, **105**, 129–146.
- Knupp, K. R., 1989: Numerical simulation of low-level downdraft initiation within precipitating cumulonimbi: Some preliminary results. *Mon. Wea. Rev.*, **117**, 1517–1529
- Mecikalski, J. R., and K. M. Bedka, 2006: Forecasting convective initiation by monitoring the 568 evolution of moving cumulus in daytime GOES imagery. *Mon. Wea. Rev.*, **134**, 49–78.
- Pryor, K.L., and G. P. Ellrod, 2004: Recent improvements to the GOES microburst products. *Wea. Forecasting*, **19**, 582–594
- Pryor, K.L., 2009: Microburst windspeed potential assessment: progress and developments. Preprints, 16th Conf. on Satellite Meteorology and Oceanography, Phoenix, AZ, Amer. Meteor. Soc.
- Pryor, K. L., 2014: Downburst prediction applications of meteorological geostationary satellites. *Proc. SPIE Conf. on Remote Sensing of the Atmosphere, Clouds, and Precipitation V*, Beijing, China, doi:10.1117/12.2069283.
- Pryor, K. L., 2015: Progress and Developments of Downburst Prediction Applications of GOES. *Wea. Forecasting*, **30**, 1182–1200.
- Przybylinski, R.W., 1995: The bow echo. Observations, numerical simulations, and severe weather detection methods. *Wea. Forecasting*,

10, 203-218.

Rabin, R., P. Bothwell, and S. Weiss, 2017: Temperature deviation from Equilibrium Temperature: Convective Overshoot from Satellite Imagery. [Available online at <http://overshoot.nssl.noaa.gov/>.]

Schmetz, J., S. A. Tjemkes, M. Gube, and L. van de Berg, 1997: Monitoring deep convection and convective overshooting with METEOSAT. *Adv. Space Res.*, **19**, 433–441.

Soden, B.J. and F.P. Bretherton, 1996: Interpretation of TOVS water vapor radiances in terms of layer-average relative humidities: Method and climatology for the upper, middle,

and lower troposphere. *J. Geophys. Res.*, **101**, 9333-9343.

Sorbjan, Z., 1989: Structure of the atmospheric boundary layer. Prentice Hall, 317pp.

Srivastava, R.C., 1985: A simple model of evaporatively driven downdraft: Application to microburst downdraft. *J. Atmos. Sci.*, **42**, 1004–1023.

Srivastava, R.C., 1987: A model of intense downdrafts driven by the melting and evaporation of precipitation. *J. Atmos. Sci.*, **44**, 1752-1773.

Wakimoto, R.M., 1985: Forecasting dry microburst activity over the high plains. *Mon. Wea. Rev.*, **113**, 1131-1143.

Acknowledgements

The author thanks the NOAA Air Resources Laboratory/Field Research Division for the Idaho National Laboratory surface weather observation data used in this research effort. The author also thanks Mr. Walter Wolf (NOAA/NESDIS/STAR) for the access to GOES-16 ABI datasets used and visualized in this paper, Dr. Tamas Varnai (University of Maryland, Baltimore County, Department of Physics) for his instruction and

guidance with Python code development and algorithm implementation, and Mr. Greg Blumberg (University of Oklahoma, School of Meteorology) for his guidance and assistance with implementation of SHARPPy.

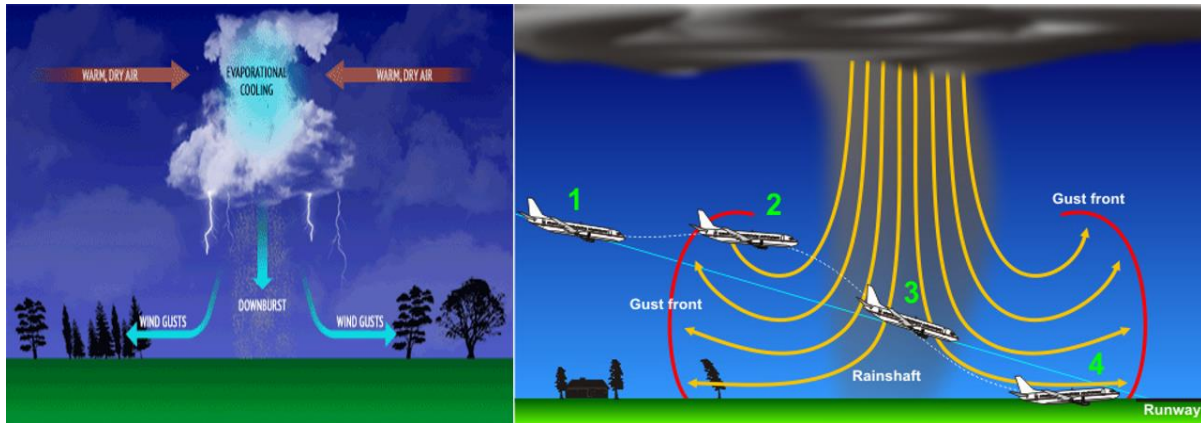


Figure 1. a) Graphical description of the physical process of downburst generation and associated outflow wind field (left) and the impact of a downburst on an aircraft on approach to a runway during landing (right).

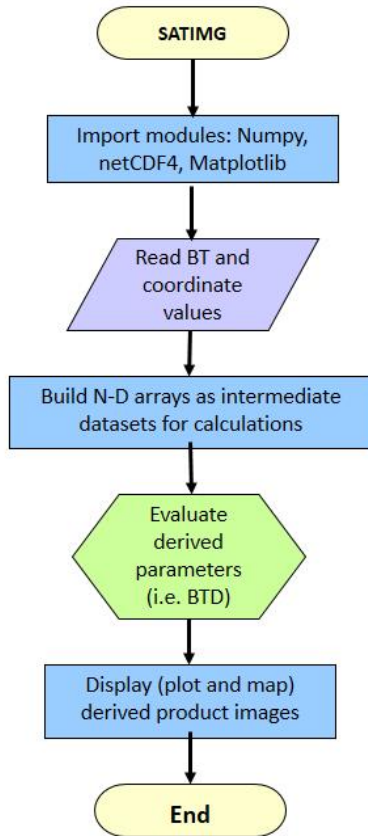
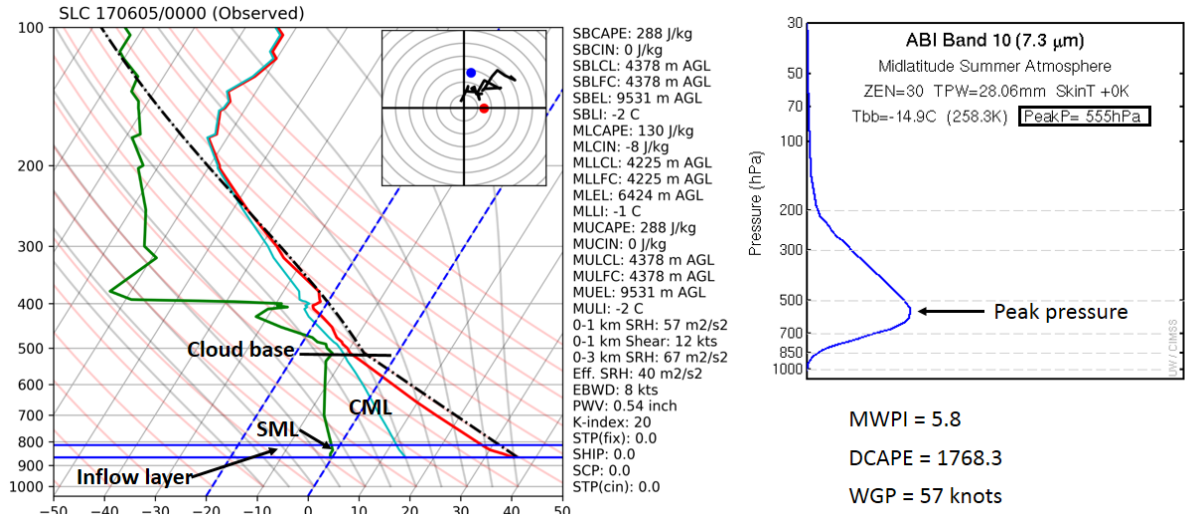


TABLE 1. Summary of the wavelengths, resolution, and sample use and heritage instrument(s) of the ABI bands. The minimum and maximum wavelength range represent the full width at half maximum (FWHM or 50%) points. [The Instantaneous Geometric Field Of View (IGFOV).]

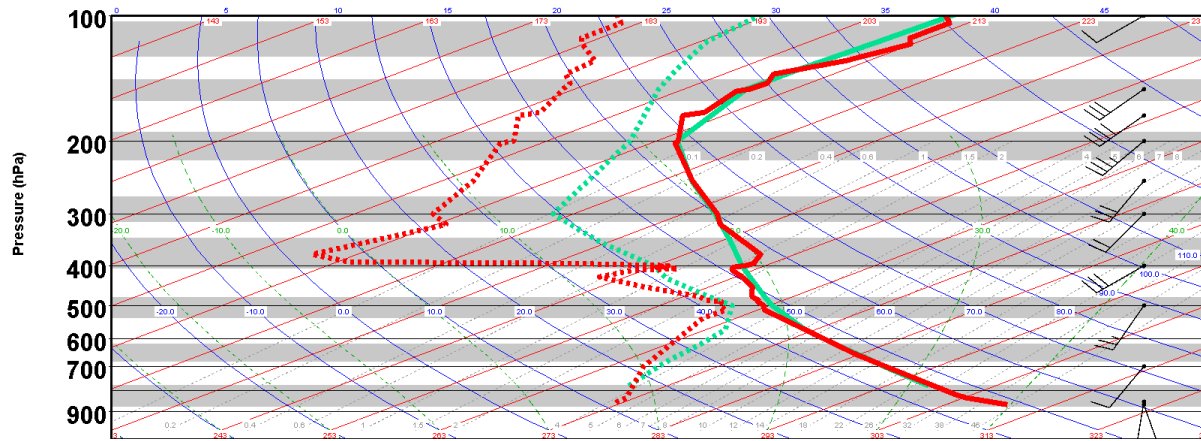
Future GOES imager (ABI) band	Wavelength range (μm)	Central wavelength (μm)	Nominal subsatellite IGFOV (km)	Sample use	Heritage instrument(s)
1	0.45–0.49	0.47	1	Daytime aerosol over land, coastal water mapping	MODIS
2	0.59–0.69	0.64	0.5	Daytime clouds fog, insolation, winds	Current GOES imager/sounder
3	0.846–0.885	0.865	1	Daytime vegetation/burn scar and aerosol over water, winds	VIIRS, spectrally modified AVHRR
4	1.371–1.386	1.378	2	Daytime cirrus cloud	VIIRS, MODIS
5	1.58–1.64	1.61	1	Daytime cloud-top phase and particle size, snow	VIIRS, spectrally modified AVHRR
6	2.225–2.275	2.25	2	Daytime land/cloud properties, particle size, vegetation, snow	VIIRS, similar to MODIS
7	3.80–4.00	3.90	2	Surface and cloud, fog at night, fire, winds	Current GOES imager
→ 8	5.77–6.6	6.19	2	High-level atmospheric water vapor, winds, rainfall	Current GOES imager
9	6.75–7.15	6.95	2	Midlevel atmospheric water vapor, winds, rainfall	Current GOES sounder
→ 10	7.24–7.44	7.34	2	Lower-level water vapor, winds, and SO ₂	Spectrally modified current GOES sounder
11	8.3–8.7	8.5	2	Total water for stability, cloud phase, dust, SO ₂ , rainfall	MAS
12	9.42–9.8	9.61	2	Total ozone, turbulence, and winds	Spectrally modified current sounder
13	10.1–10.6	10.35	2	Surface and cloud	MAS
→ 14	10.8–11.6	11.2	2	Imagery, SST, clouds, rainfall	Current GOES sounder
→ 15	11.8–12.8	12.3	2	Total water, ash, and SST	Current GOES sounder
16	13.0–13.6	13.3	2	Air temperature, cloud heights and amounts	Current GOES sounder/GOES-12+ imager

Source: Schmit, T.J., Gunshor, M.M., Menzel, W.P., Gurka, J.J., Li, J., Bachmeier, A.S., 2005. Introducing the Next-Generation Advanced Baseline Imager on GOES-R. Bulletin of the American Meteorological Society, v. 86, p. 1079-1096.

Figure 2. Flowchart illustrating the operation of Python programs that generate GOES derived product images (left) and Table 1 from Schmit et al. (2005) that summarizes the use of GOES-16 ABI bands in derived product image generation (right). Arrows indicate the bands employed in the GOES microburst prediction algorithms.



NOAA Products Validation System (NPROVS)
 Dewpoint / Temperature (deg K)



SONDE 72572 (182) SONDE 6/4/2017 23:06:00Z 40.8 N / 112 W
GOES 6/4/2017 23:07:43Z (0 hours) 40.7 N / 111.8 W (16.5 km)

Figure 3. Radiosonde observation (RAOB) thermodynamic profile over Salt Lake City, Utah at 0000 UTC 5 June 2017 (top left) compared to a GOES-16 ABI example transmittance weighting function (top right) for band 10 over southeastern Idaho; NOAA Products Validation System (NPROVS) comparison of the SLC RAOB and co-located GOES-15 sounding profile at the actual observation time (2306 UTC 4 June 2017). In the RAOB profile (top left), the vertical axis is labeled in units of pressure (mb) and the horizontal axis is labeled in units of temperature ($^{\circ}$ C). “CML” represents the convective mixed layer and “SML” represents the surface moist layer. The example transmittance weighting function is courtesy of University of Wisconsin/CIMSS.

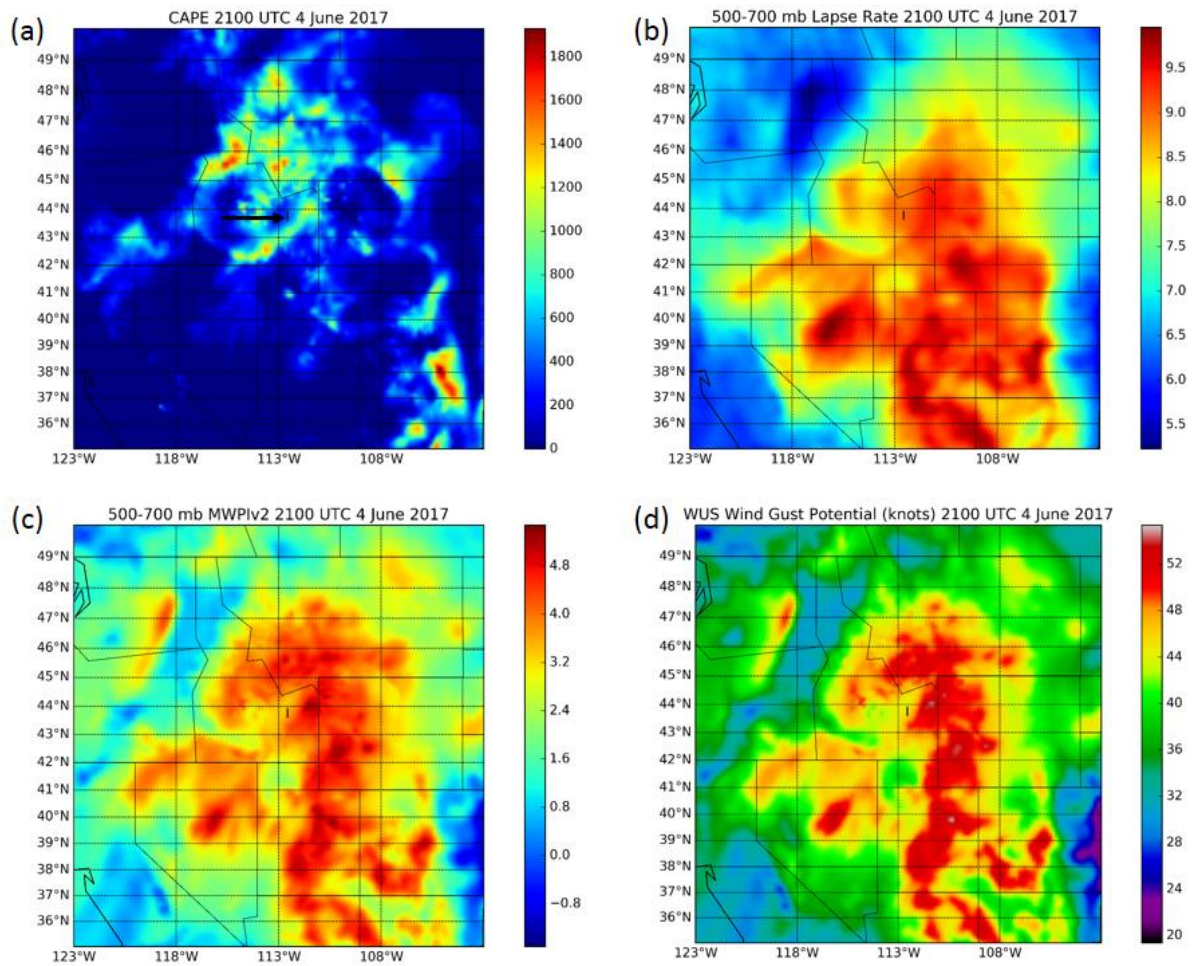


Figure 4. 2100 UTC 4 June 2017 Rapid Refresh (RAP) model derived product images: a) CAPE, b) 500 – 700 mb temperature lapse rate, c) MWPI, and d) MWPI-derived wind gust potential. “I” marks the location of the Idaho National Laboratory.

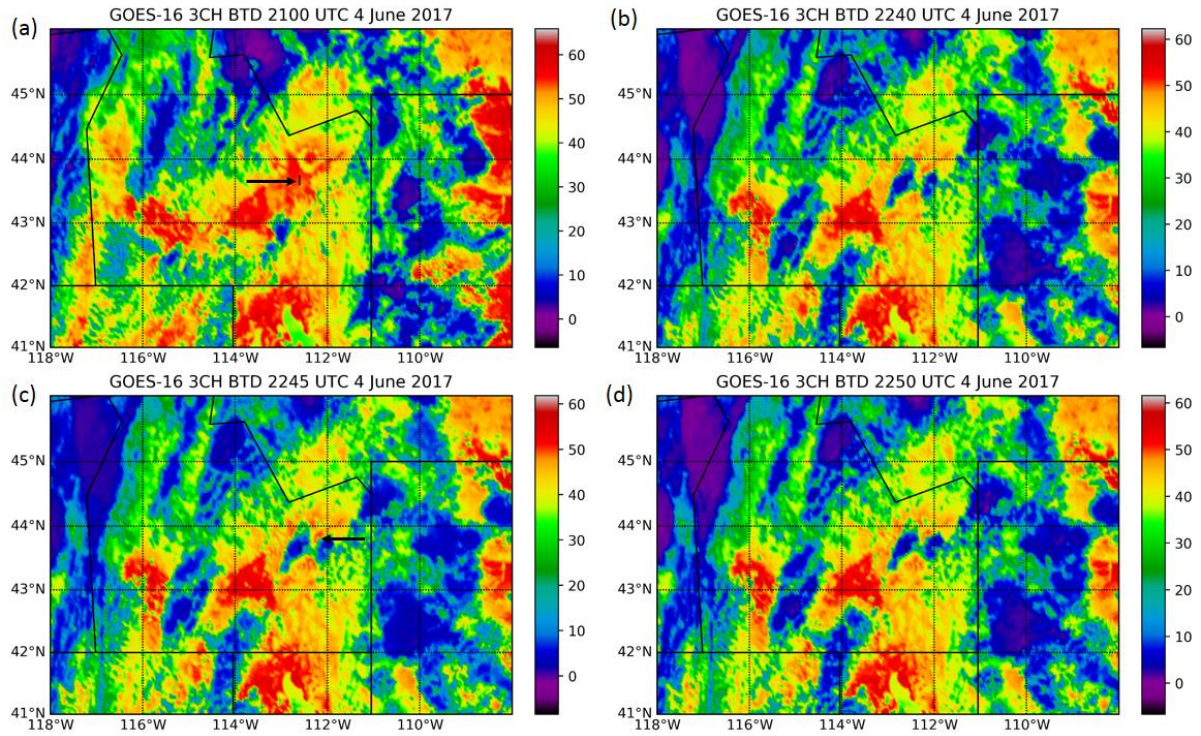


Figure 5. 4 June 2017 GOES-16 ABI three-channel BTM product images at a) 2100, b) 2240, c) 2245, and d) 2250 UTC. "I" marks the location of the Idaho National Laboratory. Black arrow in c) marks a local maximum in output BTM.

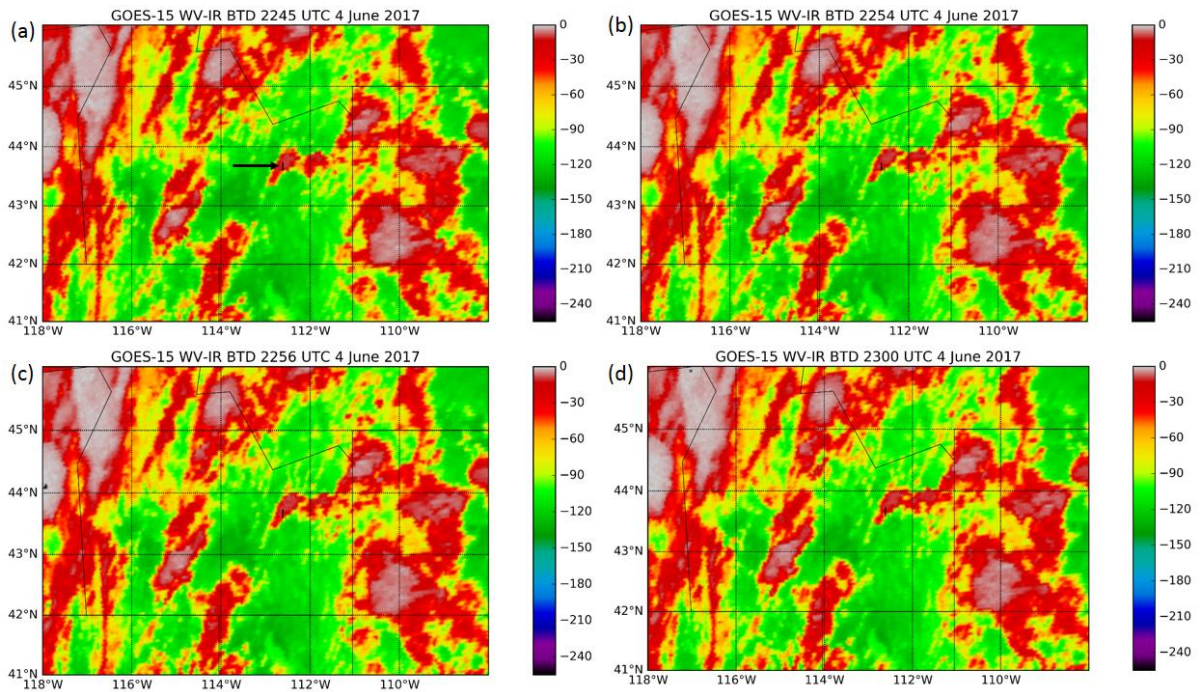


Figure 6. 4 June 2017 GOES-15 WV-IR BTM product images at a) 2245, b) 2254, c) 2256, and d) 2300 UTC. "I" marks the location of the Idaho National Laboratory.

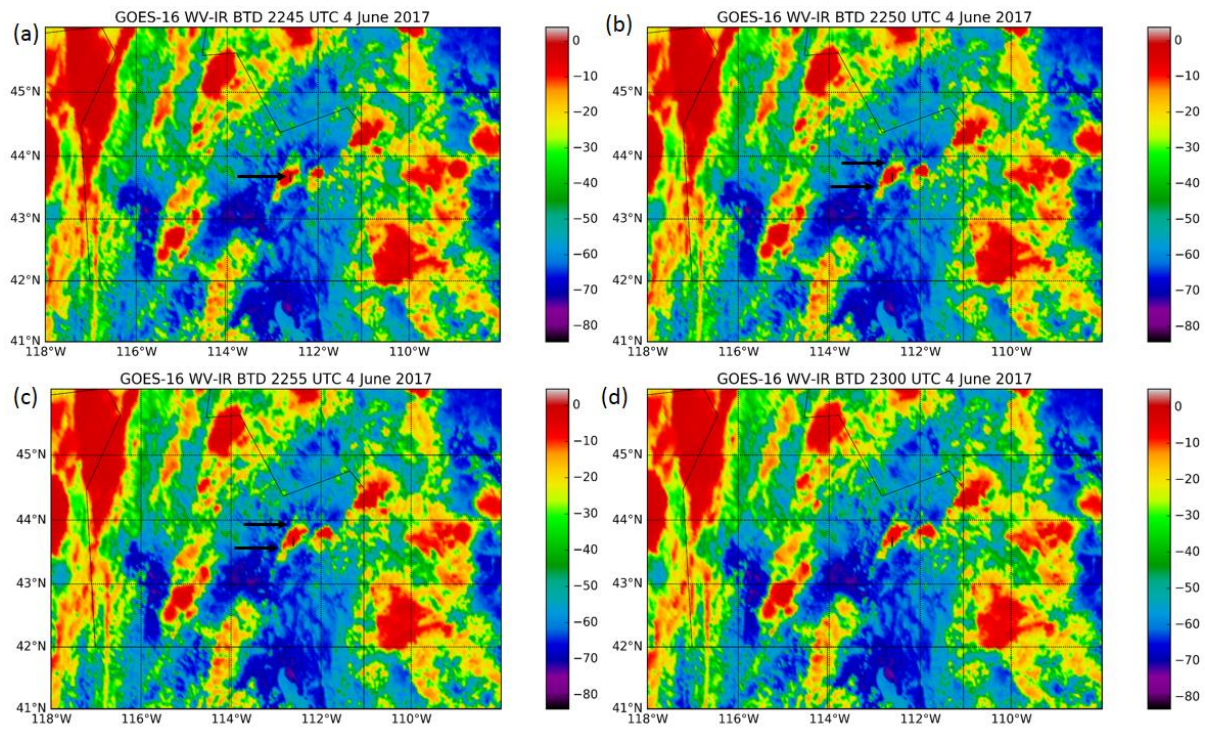


Figure 7. 4 June 2017 GOES-16 WV-IR BT product images at a) 2245, b) 2250, c) 2255, and d) 2300 UTC. "I" marks the location of the Idaho National Laboratory. Black arrows in b) and c) mark the location of dry-air notches.

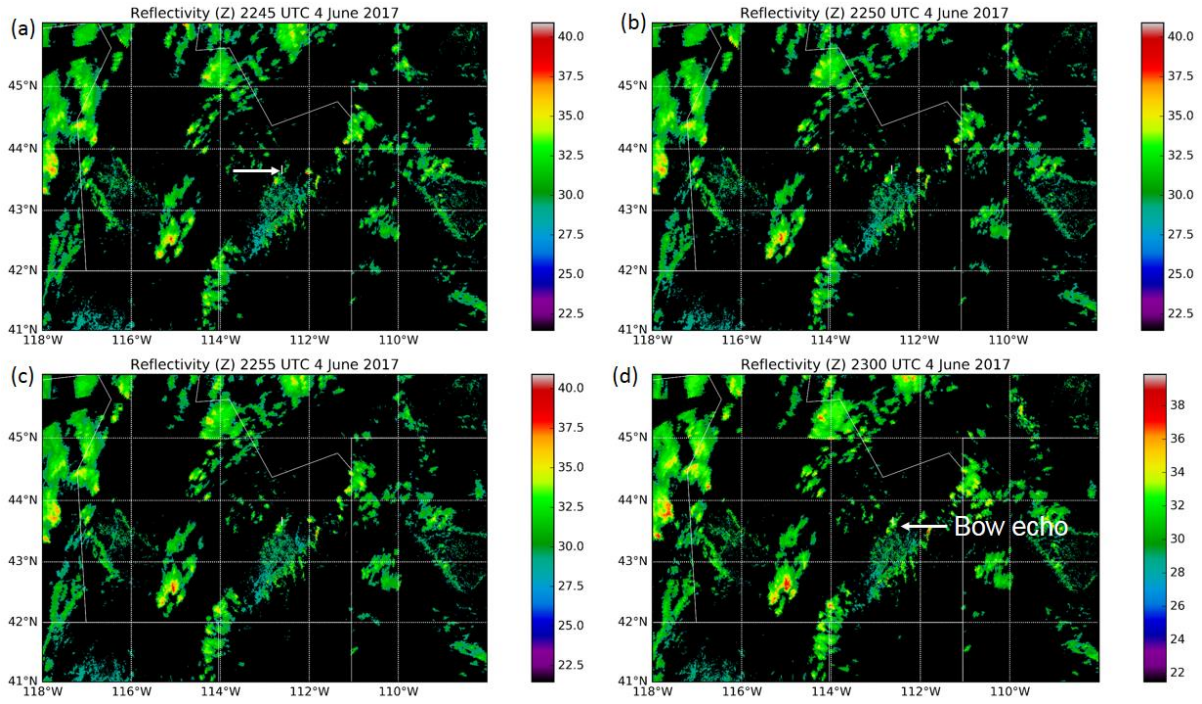


Figure 8. 4 June 2017 NEXRAD Level 3 1-km resolution base reflectivity at a) 2245, b) 2250, c) 2255, and d) 2300 UTC. “I” marks the location of the Idaho National Laboratory.

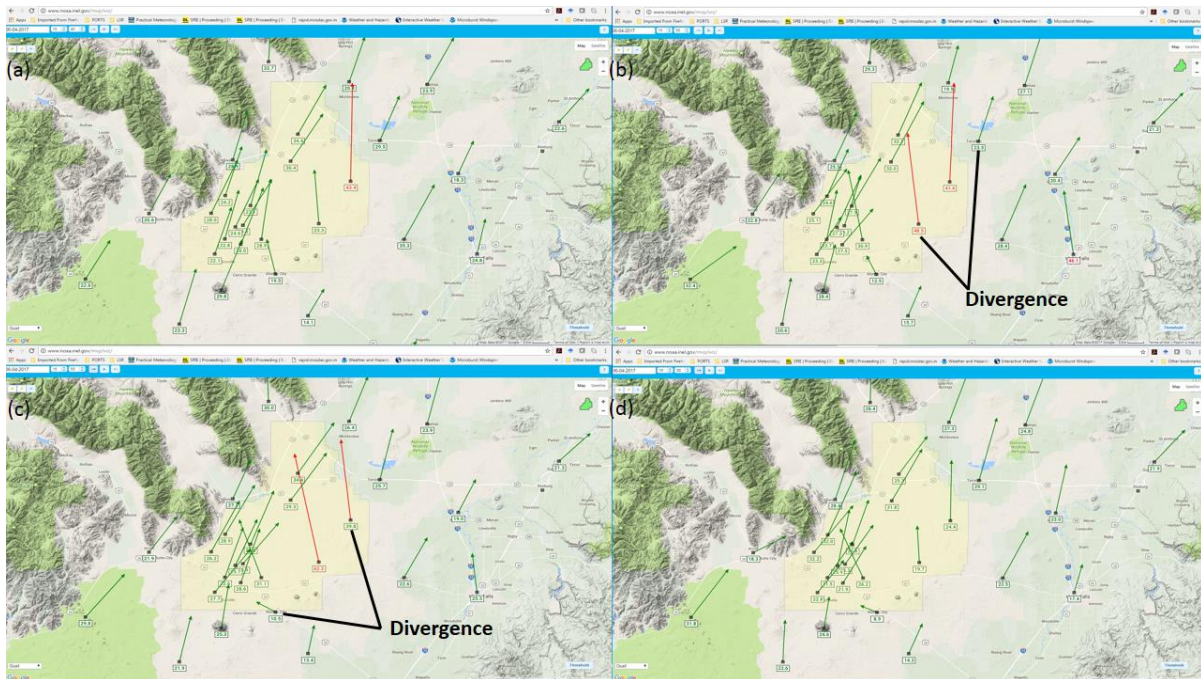


Figure 9. Map-view plots of INL mesonet surface wind observations at a) 2245 UTC (1545 MST), b) 2250 UTC (1550 MST), c) 2255 UTC (1555 MST), and d) 2300 UTC (1600 MST).

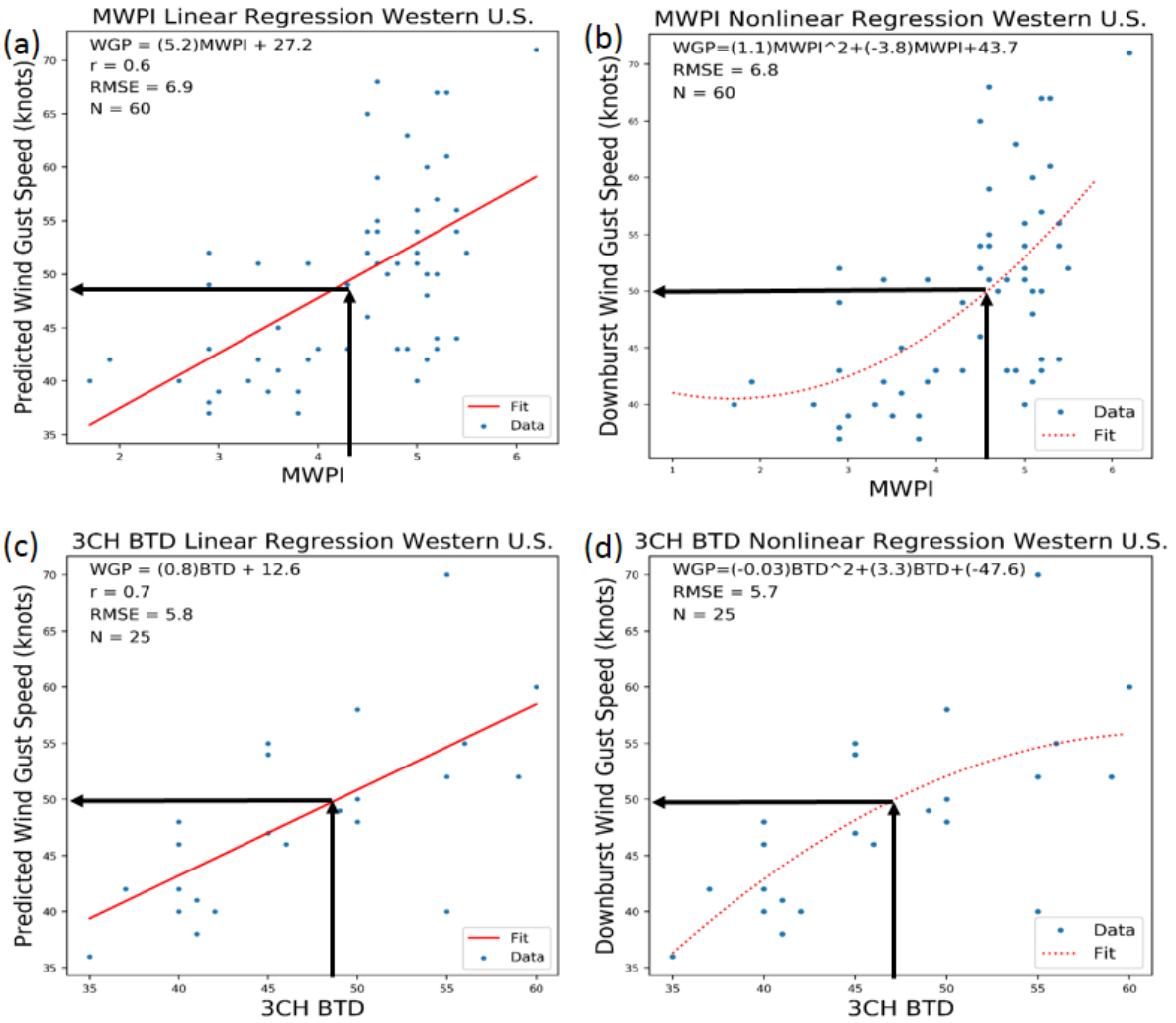


Figure 10. Statistical analysis of validation data (index values, measured wind speeds) over the U.S. Great Basin region: a) MWPI linear regression for 60 downburst events between 2013 and 2015, b) MWPI nonlinear (quadratic) regression for 60 downburst events between 2013 and 2015, c) three-channel BTD linear regression for 25 downburst events over the Idaho National Laboratory (INL) mesonet domain between 2007 and 2008, and d) three-channel BTD nonlinear (quadratic) regression for 25 downburst events over the INL mesonet domain between 2007 and 2008. “WGP” represents wind gust potential derived from the index value, “r” represents correlation coefficient, and “RMSE” represents root mean square error value.